International Journal of Biological Macromolecules 313 (2025) 144187

Contents lists available at ScienceDirect

International Journal of Biological Macromolecules

journal homepage: www.elsevier.com/locate/ijbiomac

Beyond thermal protection: Injectable self-healing chitosan hydrogel in liver tumor thermal ablation

Lifei Huang [a], Erpeng Qi [b], Zhihan Liu [a], Quanrui Zhang [a], Shuo Wang [a], Shaowei Zheng [a], Wensheng Xie [a], Guofeng Li [a], Xue Chen [a], Hui Sun [b,c,*], Fangyi Liu [b,**], Xing Wang [a,**]

[a] State Key Laboratory of Organic-Inorganic Composites, Beijing Laboratory of Biomedical Materials, Beijing University of Chemical Technology, Beijing 100029, China
[b] Department of Interventional Ultrasound, The Fifth Medical Center, Chinese PLA General Hospital, Beijing 100853, China
[c] Department of Hepatology, Tongliao Sixth People's Hospital, Tongliao 028000, China

ARTICLE INFO

Keywords:
Self-healing chitosan hydrogel
Thermal ablation
Hemostasis
Anti-tumor metastasis
Anti-tissue adhesion

ABSTRACT

Thermal ablation technology is crucial for treating early-stage primary tumors. However, the "water isolation" during clinical surgery is limited by unstable thermal protection caused by fluid loss. More seriously, it is prone to intraoperative bleeding, cancer cell metastasis, and postoperative tissue adhesion. Here we introduce a "one stone, four birds" strategy, which utilizes a self-healing chitosan hydrogel without drug assistance to offer four abilities, including thermal protection, hemostasis, anti-tumor metastasis and anti-tissue adhesion. A rabbit VX2 liver transplantation tumor model is established. The self-healing chitosan hydrogel, crosslink of hydroxyethyl chitosan (HC) and dual aldehyde-PEG (Ald-PEG-Ald) using dynamic Schiff base, adheres to the liver surface and remains *in situ* upon minimally invasive injection, resulting in outstanding thermal protection compared with saline. The temperature of the isolated tissue near the ablation foci remains below 42 °C. Moreover, the self-healing property of the hydrogel can prevent cell leakage during the procedure, thus avoiding intraoperative bleeding, tumor metastasis and postoperative abdominal adhesion. Therefore, this work identified four efficacies of the self-healing chitosan hydrogel in thermal ablation of metastatic liver tumors, providing an advanced alternative for clinical application.

1. Introduction

Thermal ablation is a crucial therapeutic technique in interventional oncology, especially for early primary tumors and oligometastatic tumors (those with three or fewer lesions) with minimal invasiveness and high technical success rate [1–5]. Currently, the mature thermal ablation technologies include Radiofrequency Ablation (RFA) [6,7], Microwave Ablation (MWA) [7,8], Laser-Induced Interstitial Thermotherapy (LITT) [9], and Cryotherapy [10]. Among them, MWA is superior for large tumors, locations around large vessels, and high perfusion areas with limited radiofrequency power [8]. Microwave energy generates faster heating and higher temperatures, leading to broader areas of necrosis [11–15]. Additionally, better defined ablation areas can be yielded in the MWA [16]. Despite MWA currently being considered an effective technique for local tumor treatment, postoperative complications such as pain, bleeding, tumor metastasis, tissue adhesion and infection are inevitably encountered [6,17–21]. Zensen et al. collectively analyzed 7228 cases of liver tumor ablation from 136 centers in Germany and Austria, revealing an overall complication rate of 3.0 % (214/7228) [22].

In clinical thermal ablation, adjunctive thermoprotective agents are often required to safeguard surrounding healthy tissue. The "water isolation" technique is commonly employed to reduce potential damage to nearby structures and minimize complications [23–28]. Saline or 5 % glucose solution is injected between the target lesion and adjacent tissues or organs to shield them from potential thermal injury [29,30]. However, its drawbacks are susceptibility to volume loss and unstable thermal protection effect. Since continuous injections are required, posing potential risks such as edema and electrolyte imbalances. Consequently, there is a pressing need in clinic for superior options to saline to implement better protection. Recent studies have developed several thermal protection hydrogels and evaluated its feasibility as substitutes for traditional liquids [31–36]. Ren et al. developed a hyaluronic acid-based hydrogel (HA-Dc) and exhibited thermal protection

* Correspondence to: H. Sun, Department of Interventional Ultrasound, The Fifth Medical Center, Chinese PLA General Hospital, Beijing 100853, China.
** Corresponding authors.
E-mail addresses: SunHuiTL@163.com (H. Sun), fangyi0317@163.com (F. Liu), wangxing@mail.buct.edu.cn (X. Wang).

https://doi.org/10.1016/j.ijbiomac.2025.144187
Received 6 March 2025; Received in revised form 8 May 2025; Accepted 12 May 2025
Available online 14 May 2025

performance for thermal ablation [37]. While complications associated with clinical tumor ablation extend beyond thermal damage, encompassing potential issues such as bleeding, adhesions and tumor implantation, which require a systematic assessment.

For this purpose, we proposed a treatment strategy of "one stone, four birds" in this study, that is, utilizing an injectable self-healing chitosan hydrogel to evaluate the comprehensive effect of thermal ablation therapy of the hydrogel in the established rabbit VX2 highly metastatic liver tumor model. The specific self-healing chitosan hydrogel is formed based on the dynamic Schiff base between biocompatible Hydroxyethyl Chitosan (HC) and dual aldehyde-PEG (Ald-PEG-Ald), which endows the chitosan hydrogel injectability and shape adaptability. We aimed to achieve multiple goals with one intervention: the injectable self-healing chitosan hydrogel for thermal protection, hemostasis, anti-metastasis and anti-adhesion in tumor thermal ablation (Scheme 1). Compared with saline, the self-healing chitosan hydrogel exhibits superior *in-situ* retention. Its self-healing properties facilitate rapid healing of hydrogel gaps formed during surgical procedures, thus blocking the leakage of blood cells and tumor cells, then inhibiting tumor metastasis and potential postoperative tissue adhesion. We believe that this self-healing chitosan hydrogel holds significant advances in clinical adjunctive MWA treatment, not only effective for existing early-stage oligometastatic tumors, but also applicable to high metastatic tumors.

2. Materials and methods

2.1. Materials

Hydroxyethyl Chitosan (HC, 82 kDa, Wako Pure Chemical Industries, Ltd., Japan). Dual aldehyde-PEG (Ald-PEG-Ald, Mn ≈ 4000 g/mol) was prepared according to the experimental protocol reported [38]. L929 cells were acquired from Servicebio Co., Ltd. (Wuhan, China). RPMI 1640 medium (RPMI 1640), penicillin-streptomycin (PS) and trypsin were purchased from Gibco Life Technologies (Beijing, China). Fetal bovine serum (FBS) was purchased from Sigma. All solvents were purchased from Sinopharm Chemical Reagent and used directly without further purification. The animal experiments were performed using rabbits weighing 3.5–4.2 kg, which were provided by Beijing Jinmuyang Experimental Animal Breeding Co., Ltd. The experimental animal protocols were carried out following Beijing (China) Animal Experiment Guidelines (2010) and were authorized by the ethics committee of The Fifth Medical Center, Chinese PLA General Hospital (Approve number: 2023-X-19-91).

2.2. Preparation and microstructure analysis of the hydrogel

2.5 % hydrogel was prepared by mixing 3 mL 3 % HC with 1 mL 1 % Ald-PEG-Ald solutions at room temperature. The sol-gel transition was confirmed when no visual flow was observed after tilting the vial for 30 s, with Acid Orange 7 used to stain the hydrogel for visualization. To observe the microstructure, the hydrogel was freeze-dried to obtain dry

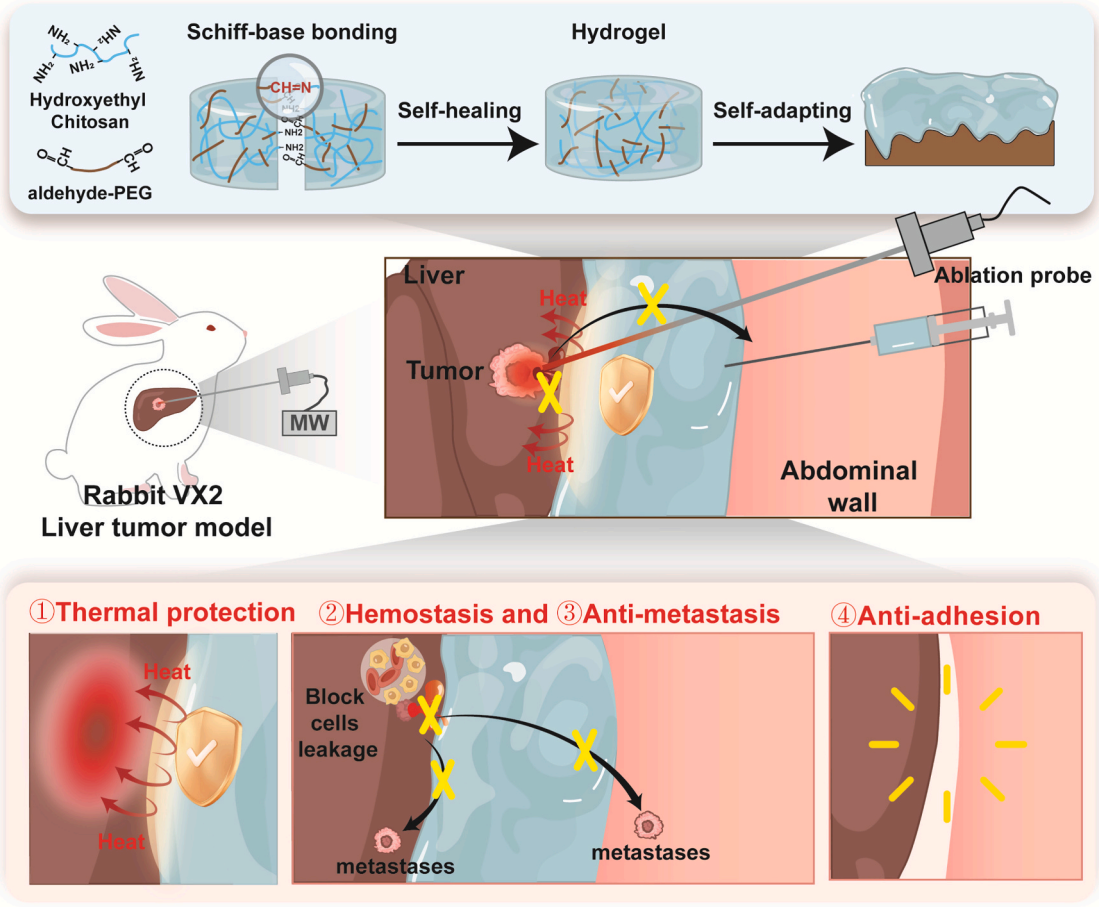

Scheme 1. Schematic illustration of the structure of self-healing chitosan hydrogel and the protocol: using a self-healing chitosan hydrogel for thermal protection, hemostasis, anti-metastasis, and anti-adhesion.

hydrogel sample. The sample were gold-plated and then imaged using a scanning electron microscope (SEM) (ZEISS, Supra 55, German) with an accelerating voltage of 5 kV.

2.3. Rheological analysis and injectability

The shear thinning behavior of hydrogel was assessed using a TA rotational rheometer (TA Discovery HR 30, USA). Tests were carried out on parallel plates with a diameter of 16.5 mm. The stability of the hydrogel was determined by frequency sweep tests at 25 °C, 1 % constant strain, and a frequency of 0.1–100 rad/s. The strain sweep tests were determined at 1 % rad/s, and a strain range of 1 %–1000 %. The step strain of the hydrogel was determined by the sequential passage through 1 %, and 600 % strain at a frequency of 1 rad/s for successive periods of 180 s. Additionally, the injectability of the hydrogel (stained with Acid Orange 7) was determined by injection using a 1 mL syringe (Needle 26G).

2.4. Adhesion property

The different substrates (nitrile gloves, petri dish, glass, liver) were used to assess the adhesion properties of the hydrogel.

2.5. Self-healing property

The hydrogel was extruded from the syringe to form a shattered structure and the healing behavior of the hydrogel was observed over a period of time. Photographs were taken to record their self-healing behavior.

2.6. Hemolysis experiment

Gradient concentration dispersions were prepared by dissolving the hydrogel powder with PBS and ultrasonication for 2 h. 1 mL of blood was added to 2 mL of PBS and centrifuged at 500 g for 10 min, followed by de-conditioning of the supernatant to 10 mL (RBC solution). 0.2 mL of the above-treated RBCs were added to 0.8 mL of the different concentrations of dispersions. The samples were incubated for 3 h at 37 °C followed by centrifugation for 5 min at 10,000 g. The mixture of PBS and deionized water with RBCs was used as negative and positive control. The absorbance values were then measured at 540 nm. The hemolysis rate was calculated according to the following formula:

$$Haemolysis\ rate\ (\%) = (OD\text{sample} - OD\text{negative})/(OD\text{positive} - \text{O}D\text{negative}) \times 100\%$$

2.7. Degradation performance

For the *in vitro* hydrogel degradation test, each set was processed with PBS at 37 °C, and the degradation performance of the hydrogel was evaluated by the weight loss method. The samples were removed at a set time, dried with filter paper and weighed. The experiment was repeated three times. The *in vivo* degradation of hydrogel was assessed *via* ultrasound. Under ultrasound guidance, 4 ml of hydrogel was injected around the thyroid gland of Beagle dog, bypassing structures such as blood vessels, trachea and nerves in the neck. After injection, a distinct hypoechoic region was produced on the ultrasound image. This region was then observed and recorded daily over a seven-day period to track the degradation of hydrogel.

2.8. Biosafety assay

The CCK-8 assay was used to assess the cell viability to detect the *in vitro* toxicity of the hydrogel. L929 cells were cultured in 96-well plates with 1×10^4 cells/well. The 3 % HC and 1 % Ald-PEG-Ald solution were added to the well plates. For 2.5 % hydrogel, the original medium was removed and 100 μL of the mixed hydrogel precursor solution was added to each well. The plate was left for approximately 10 min to allow complete gelation. Then, 50 μL of liquid culture medium was added on top of each gel to ensure nutrient exchange. Subsequently, the cells were placed in a cell culture incubator for co-incubation. After adding 10 μL of CCK-8, each sample was incubated for 3 h, and then the absorbance at 450 nm was measured.

2.9. In vitro sealing test

The ability to seal blood vessels of the hydrogel was assessed by sealing testing assay [39]. A collagen cannula (diameter: 16 mm) was used as a tissue matrix. A digital manometer (HANDPI, HP-10) was attached to the end of the collagen casing for pressure measurement. Initially, PBS was filled with collagen casings until the pressure reached 70 mmHg. Then, the hydrogel was adhered to the collagen casing, which was subsequently punctured with needles of different gauges (Needle 26G and 22G) against the underside to simulate blood loss. Pressure changes were recorded by a digital manometer.

2.10. Thermal analysis of the hydrogel

A copper block with heater was used to generate a stable uniform high-temperature surface (the top of the block). A hydrogel cube with dimensions of 20 mm × 20 mm was placed on the top of the cooper block. The hydrogel cube was surrounded by insulating material on all sides to minimize heat loss and ensure one-dimensional heat conduction. Four thermocouples (Omega, TT-T-36-SLE) were used to measure the block surface temperature and hydrogel inner temperatures. The distance between monitoring points 1 and 2 was set at 7 mm, between points 2 and 3 was 5 mm, with points 3 and 4 being identical. The thermal conductivity of the hydrogel can be calculated according to Fourier's law (1).

$$Q = A\lambda\, dT/dx \tag{1}$$

Dynamic thermography was employed to visually assess heat transfer in the hydrogel and saline. The hydrogel was formed in a petri dish and a central hole was created, with the diameter of the hole matching that of the iron block. The iron block, preheated to 120 °C, was placed into the artificial holes and thermal images were recorded using an infrared camera. The saline control group underwent the identical procedure.

2.11. Construction of rabbit VX2 transplanted liver tumor model

The VX2 tumor was made into a suspension and injected about 1 mL into the muscle of the lateral thigh of rabbits [40–42]. After 1 week, anesthetize tumor bearing rabbits with a dose of Midazolam Injection (Jiangsu Nhwa Pharmaceutical Co., Ltd.): Cyperazine Hydrochloride Injection (Jilin Huamu Animal Health Products Co., Ltd) =1:1, 0.10 mg/kg, the leg tumor tissues were peeled off under aseptic conditions. The greyish-white fish-like tissue at the edge of the tumor was clipped if possible, and then the tumor mass was sheared into tissue pieces about 1

to 2 mm in diameter. After the experimental rabbits were fully anaesthetized, their limbs were fixed and the skin was prepared, a longitudinal incision of about 3 cm in length was made layer by layer at the xiphoid process along the midline of the abdomen. The liver was grasped with toothless forceps and raised into the abdominal cavity, the liver tissue was punctured with ophthalmic forceps in the thicker left central lobe of the liver, 2 pieces of the clipped tumor were implanted in it. The needle was removed and immediately compressed with a gelatin sponge block. After confirming that no significant bleeding occurred, the liver was retracted into the abdominal cavity and closed layer by layer with abdominal sutures. Subsequently, the incision was cleaned with povidone-iodine, and penicillin was injected intramuscularly with 200,000 U/kg once a day after the operation.

2.12. In vivo percutaneous liver tumor ablation protocol

After anesthesia, the rabbits were placed in the supine position. A 1–2 mm cut was made into the skin of rabbit with a sharp knife and the microwave antenna was placed at the site indicated by the ultrasound. Saline or hydrogel was injected using a 20 mL syringe (needle: 22G) to provide an isolation zone. The total injection volume of normal saline accumulated to 15 mL before and during ablation, whereas the hydrogel required only a single injection of 4 mL before ablation. The ablation was performed for 2 min at 20 W microwave power output using a MWA therapist (KY-2000, Nanjing Kangyon Medical Technology Co., Ltd.). Based on the size of the tumor, 2–3 MWA treatment cycles (20 W, 2 min) are usually required. Doppler ultrasound was used to monitor the ablation process throughout the procedure, and the temperature during ablation were recorded. Postoperatively, 200 mL of saline was injected into the abdominal cavity of rabbits, and the ascites was collected after 15 min for blood count and free tumor cells count. Blood cell counts were performed by a hematology analyzer (Mindray, China). Meanwhile, tumor cells were labeled with 7-AAD dye (Beyotime, China) and subsequently observed using fluorescence confocal. All rabbits underwent postoperative ultrasonography to assess tumor metastasis after percutaneous ablation of liver tumors.

Since the *in vivo* degradation time of the hydrogel is within 7 days, the animals were sacrificed on day 6 to examine remaining hydrogel and harvest both target and non-target tissues from the thermal injury regions. Then, photographs were taken to describe the areas of ablative damage and areas of adhesions on the tissue. The adhesion levels were recorded according to the adhesion scoring criteria system. Score 0, no adhesions; score 1, 1 thin layer of adhesions; score 2, >1 thin layer of adhesions; score 3, thicker adhesions to the focal point; score 4, thicker adhesions attached to the pedicle, which can be separated with strong blunt dissection; score 5, very thick vascular adhesions, which require sharp dissection. Blood was collected on day 1, 4 and 6 postoperatively and samples was used for aspartate aminotransferase (AST), alanine aminotransferase (ALT), alkaline phosphatase (ALP), blood urea nitrogen (BUN) and creatinine (CREA) measurements to assess liver and kidney function. All procedures were performed by clinically experienced interventional ultrasonographers.

2.13. Animal sampling and histological examination

After the animals were sacrificed on day 6, normal and heat-damaged abdominal tissues, metastatic tumor tissues, and adherent tissues of rabbits were harvested and fixed in 4 % paraformaldehyde (PFA) solution. Tissue samples were further embedded in paraffin and subjected to hematoxylin and eosin (H&E) staining, Masson staining, Ki67 and MMP2 immunostaining evaluation to assess tissue damage. Sections were visualized with a Leica microscope.

2.14. ELISA assay

Different groups of abdominal wall tissue samples were added to 9 times the volume of homogenization medium. The 10 % homogenate was prepared by mechanical homogenization under ice water bath conditions. Subsequently centrifuged at 2500–3000 rpm for 10 min and the supernatant was taken for assay. TNF-α, IL-6, IL-4, and IL-10 levels in the tissues were measured using the relevant Rat ELISA Kit (Cloud-clone CORP. Wuhan, China). The saline-treated group was used as a positive control for the thermal injury response, and the hydrogel-treated group was used as the experimental group. All experiments were repeated three times.

2.15. Quantitative Rea-time PCR (qPCR) assay

To assess the extent of thermal injury to the abdominal tissues and abdominal adhesions after surgery, the mRNA levels of heat shock protein HSP70 in the locally injured tissues and TNF-α in the adherent tissues were examined. The experimental methods are as follows: An 80–100 mg of abdominal tissue from the thermal injury site was harvested. Total RNA was extracted with 1 mL Trizol reagent and cDNA was synthesized by reverse transcription using a reverse transcription kit (Servicebio, China). A reaction system containing cDNA, 2.5 μM gene-specific primers, 2× SYBR, and Water Nuclease-Free was assayed using a real-time fluorescence quantitative PCR instrument (Bio-rad, USA). GAPDH was used as the housekeeping gene and gene expression changes were calculated by the $2^{-\Delta\Delta CT}$ assay. The control group (tissue not treated for thermal injury) was used as a normalized baseline. The relevant primer sequences are as follows: The TNF-α primer sequences were 5′-CGTAGTAGCAAACCCGCAAGT-3′ and 5′-ACCTTGTTCGGGTAGGAGACG-3′; for HSP70 were 5′-AA-GCCAGACGACAATCAGGA-3′ and 5′-CATGGCTGCAAGAACCTC-TG-3′; for GAPDH were 5′-TTCCAGTATGATTCCACCCACG-3′ and 5′-GGGCTGAGATGATGA- CCCTTTT-3′.

2.16. Statistical analysis

Statistical analysis was performed by GraphPad Prism 8.0 and Microsoft Excel. Group differences were assessed using Student's *t*-test or one-way analysis of variance (ANOVA). Statistical significance was defined as $^{*}p < 0.05$, $^{**}p < 0.01$, and $^{***}p < 0.001$.

3. Results and discussion

3.1. Characterization of the hydrogel

For the self-healing chitosan hydrogel utilized in this study, HC, with a heavy average molecular weight of about 163,481 g/mol (Fig. S1), contributes the polymer backbone of the hydrogel, and the cross-linking reaction is a typical Schiff base reaction. The sol-gel transition occurs upon complete mixing of HC and Ald-PEG-Ald solutions, transforming the transparent liquid into a homogeneous hydrogel (Fig. 1a). The reaction conditions are mild and easy to prepare large quantities samples. The hydrogel can be extruded from a 1 mL syringe (Fig. 1b). Syringe shear dilutes the hydrogel, temporarily disrupting its structure, which then self-heals into a complete disc after 30 min (Fig. 1c). The hydrogel exhibits a porous morphology that facilitates the transfer and diffusion of nutrients and therapeutic agents across tissues (Fig. 1d). Oscillatory frequency sweep tests revealed a mechanical strength of 266 Pa for the hydrogel (Fig. 1e). Oscillatory strain tests meant that the hydrogel disintegrated its hydrogel morphology at high strain (>600 %, Fig. S2). Then, the step strain sweep tests confirmed its self-healing capability that the hydrogel could be restored under low strain (1 %) after disintegration under high strain (600 %, Fig. 1f). Such reversible connections can facilitate adaptation to dynamic and complex local environments. It also shows good adhesion to various synthetic materials and organs, such as nitrile gloves, petri dish, glass, and liver (Fig. 1g), allowing to serve as a protective barrier by adhering to the surface of the organs after injection.

The hemolysis rate of the hydrogel was found to be <1 % for all

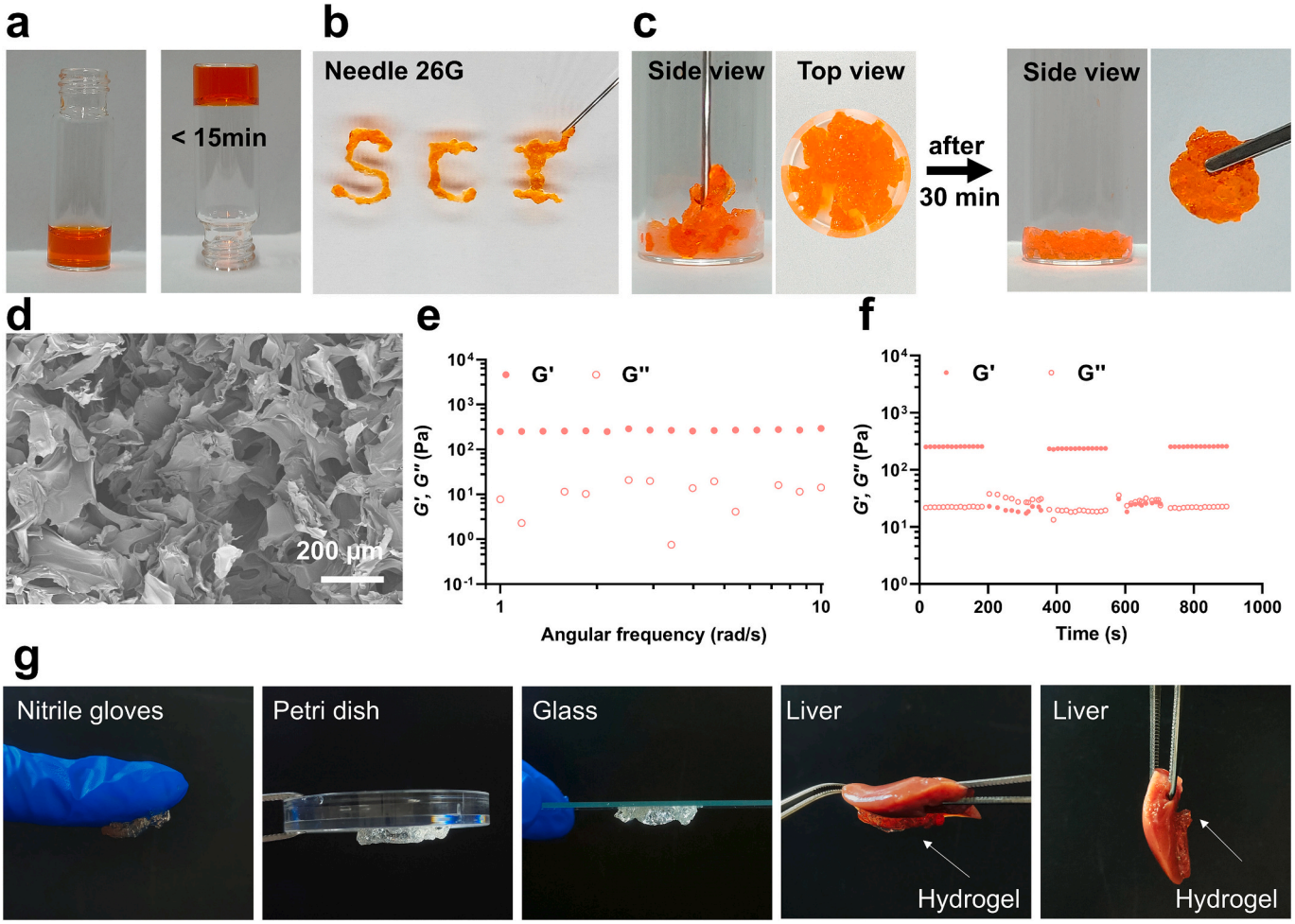

Fig. 1. Characterization of the hydrogel. (a) The formation of the hydrogel was observed by inversion of the vials. (b) Injection properties, (c) Macroscopic self-healing properties. (d) SEM images showing the microstructure of hydrogel. (e) Storage modulus G' and loss modulus G" of the hydrogel. (f) Oscillatory step-strain sweep tests of hydrogel. (g) Adhesion of the hydrogel to different substrates.

samples, which is well below the 5 % threshold for blood-contact materials in accordance with the international standard (ISO/TR7405) (Fig. S3). Cytotoxicity tests using the CCK-8 assay showed that the cell viability for both 1 % Ald-PEG-Ald solution, 3 % HC solution and 2.5 % hydrogel was above 80 % (Fig. S4), suggesting high cytocompatibility. Further, the hydrogel was sufficiently degraded within 40 h in a PBS environment simulating peritoneal ascites (Fig. S5), demonstrating rapid metabolism without burden to the organism. Furthermore, the *in vivo* degradation of the hydrogel was monitored by ultrasound (Fig. S6). The results showed that the hydrogel formed a hypoechoic region (d1:1 cm, d2:2.34 cm) around the thyroid gland on day 1. The hypoechoic region was seen to narrow significantly (d1:0.62 cm, d2:1.07 cm) on day 4. Eventually on day 7, no hypoechoic areas were observed, indicating that the hydrogel could be degraded within 7 days *in vivo*. Hence, the hydrogel is blood-compatible, non-cytotoxic, and degrade rapidly both *in vitro* and *in vivo*, supporting its safety and efficacy for *in vivo* applications.

3.2. *Thermal protection of the hydrogel in percutaneous ablation of tumors*

The thermal insulation efficacy was evaluated in an *in vivo* rabbit VX2 liver tumor model. Fig. 2a presents a schematic of the MWA protocol. The volume and morphology of VX2 transplanted liver tumors in rabbits were assessed using ultrasonography (US). Ultrasound images reveal a regular, spherical tumor shape in a diameter of 1.69 cm, with low blood flow within the tumor and abundant peripheral blood flow (Fig. 2b, Fig. S7). During percutaneous tumor ablation, saline (Video 1) and hydrogel (Video 2) were injected separately as physical barriers to provide thermal protection to the tissue around the ablation foci. A separation distance of 7.0 mm was achieved by injecting 4 mL of hydrogel, compared with only 3.6 mm after 15 mL of saline injection. The hydrogel achieves approximately 2-fold higher separation distances than saline *in vivo*, while requiring only 27 % volume fraction (Fig. S8, Video 3, Video 4). The area of the isolation zone formed by saline was about 0.99 cm^2, and the area of hydrogel was about 1.11 cm^2 (Fig. 2c, Fig. 2d). During the procedure, the area of saline was reduced to 0.98 cm^2, requiring constant replenishment and adding complexity to the surgical procedure. In contrast, the area of the hydrogel was reduced to 1.05 cm^2, and only 4 mL of hydrogel was injected at once before the operation without additional replenishment, greatly reducing the operation complexity. The hydrogel remains stable before, during and immediately after ablation, demonstrating excellent retention at the focal site. During the procedure, saline carried away part of the heat. However, the monitoring temperature of the abdominal wall tissue exceeded 55 °C with raised risk of abdominal wall injury and post-operative adhesions. (Fig. 2e). The temperature of the abdominal wall was controlled below 42 °C in the hydrogel group. There is virtually no thermal damage to the tissue at this temperature which confirmed by temperature monitor. The saline group gradually increased temperature with ablation time, while the hydrogel group stabilized at approximately 42 °C within 2 min of ablation (Fig. 2f). Thus, the hydrogel as a

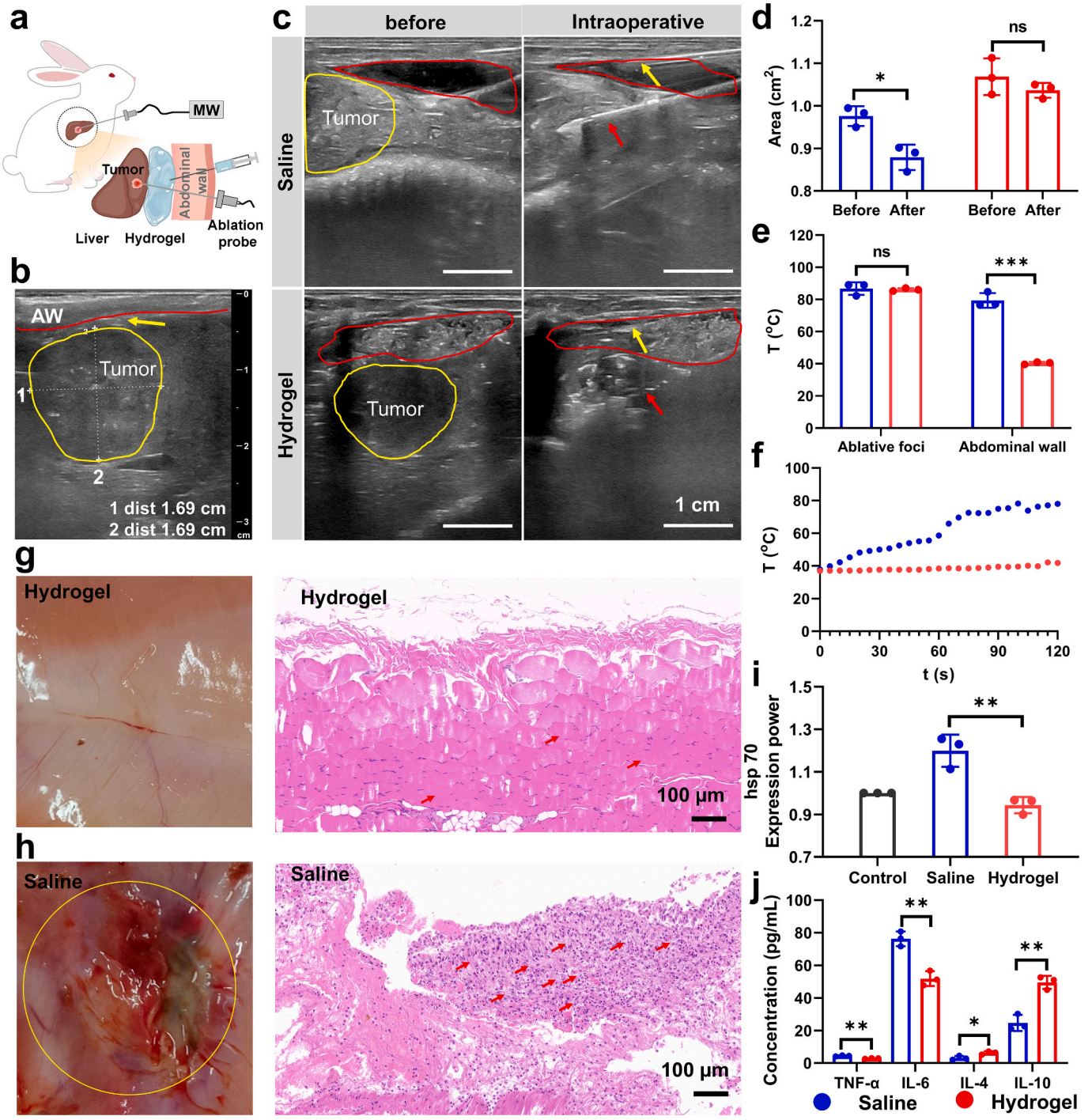

Fig. 2. Thermal protection of the hydrogel in percutaneous ablation of tumors. (a) Graphic illustration of the MWA therapy protocol. (b) Ultrasonic image of transplanted liver VX2 tumor. The tumor is denoted by the yellow circle. The yellow arrow denotes the location of the isolation agent. The red area refers to the abdominal wall. (c) Ultrasonic images of injecting saline and hydrogel respectively between liver and abdominal wall before and during MWA therapy. The tumor is denoted by the yellow circle. The isolation zone is denoted by the red circle. The red arrow represents the ablation antenna. The yellow arrow represents the temperature antenna. Scale bar: 1 cm. (d) Statistics of isolation area for saline and hydrogel before and after MWA therapy. (e) Temperature statistics of the ablation foci and abdominal wall for saline and hydrogel during operation. (f) The process of temperature curve over time of the abdominal wall during surgery. Pictures and H&E staining of rabbit abdominal wall tissue postoperatively in the saline (g) and the hydrogel groups (h). The arrow shows the accumulation of inflammatory cells. Scale bar: 100 μm. (i) HSP70 mRNA expression levels in rabbit abdominal wall tissues after surgery. (j) ELISA analysis of relevant inflammatory factors (TNF-α, IL-6, IL-4, IL-10) in postoperative rabbit abdominal wall tissues. The results are expressed as the mean ± SD in all groups ($n = 3$). ns indicates no difference in data, $^{*}p < 0.05$, $^{**}p < 0.01$, $^{***}p < 0.001$.

physical barrier for percutaneous tumor thermal ablation significantly reduces the prognosis for abdominal wall injury.

After surgery, the experimental rabbits were immediately sacrificed and the abdominal wall tissue surrounding the ablation foci was harvested. No visible changes were observed in the abdominal wall tissue of the hydrogel group (Fig. 2g), whereas significant damage was noted in the saline group (Fig. 2h). Histological results displayed sparse and disorganized cell arrangement in the saline group tissue, with

substantial accumulation of inflammatory cells (denoted by arrows). HSP70 is typically expressed at low levels in cells but its expression increases significantly in response to elevated temperature and various harmful stresses. The expression levels of HSP70 in local tissue were detected by qPCR, revealing significantly higher levels in the saline group than the hydrogel group (Fig. 2i). The H_2S levels of the tissue corroborates this finding, as H_2S is a gaseous inflammatory signaling molecule [43,44]. The H_2S level was increased in the saline group, while there was no significant increment in the hydrogel group (Fig. S9). Following peritoneal damage, pro-inflammatory cytokines (TNF-α, IL-6) are released by injured mesothelial cells and inflammatory cells. The levels of inflammatory factors in the local tissues of the ablation foci were assessed by ELISA (Fig. 2j). The overall levels of pro-inflammatory cytokines TNF-α and IL-6 were significantly higher in the saline group. In comparison, the expression of anti-inflammatory cytokines (IL-4, IL-10) was increased after hydrogel treatment. In other words, the hydrogel effectively mitigates the surgery-induced inflammatory response, which is consistent with the thermal protection effect it plays as described above.

3.3. Heat transfer analysis of the hydrogel

The observed *in vivo* thermal protection efficacy prompted us to systematically investigate the intrinsic thermal conductivity of hydrogel as a potential key determinant of its performance. The heat transfer analysis setup is shown in the Fig. 3a. The hydrogel was filled in a cubic mold surrounded by insulating material on all sides (Fig. 3b), underneath the hydrogel was a heating table (Fig. 3b insert image) with a height of 3 mm (Fig.S10). The distance between monitoring points 1 and 2 was set at 7 mm, between points 2 and 3 was 5 mm, with points 3 and 4 being identical (Fig. 3c). In Fig. 3d, the upper surface of the copper block was heated and maintained at 100 °C, and the hydrogel cube was then placed on it. The temperature increased 14.4 °C at point 2 in 2 min. It did not exceed the limit temperature (42 °C) within 2 min (coinciding with

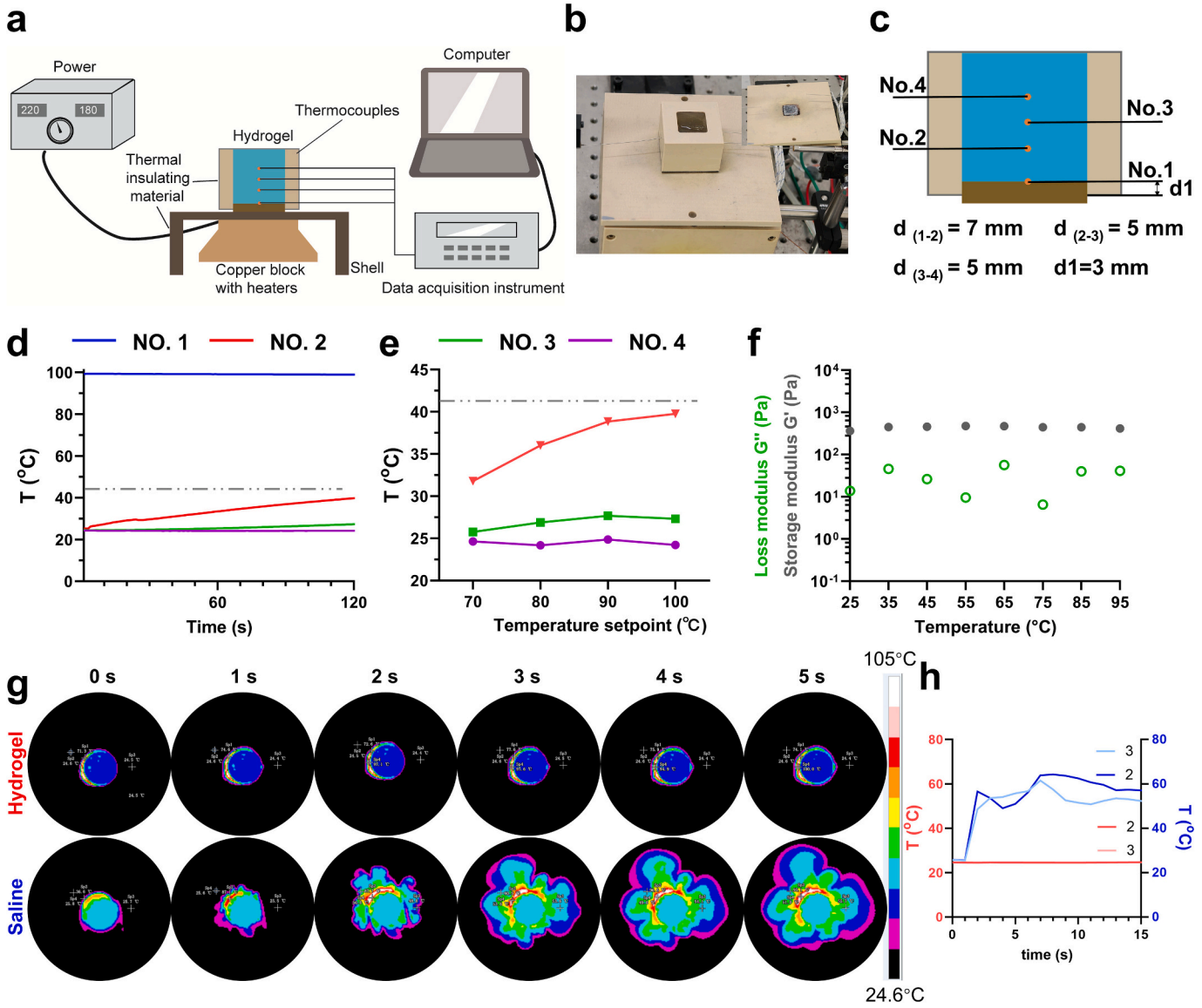

Fig. 3. Thermal analysis of the hydrogel. (a) Experimental schematic diagram of thermal properties of hydrogel. (b) Photographs of the experimental set-up and heating table (insert image). (c) Schematic of the location of the thermocouple line monitoring point inside the hydrogel. (d) Temperature variation at each monitoring points inside the hydrogel when the heater is 100 °C. (e) The steady-state temperatures at each monitoring point at 2 min under set temperatures of 70 °C, 80 °C, 90 °C, and 100 °C. The dashed gray line indicates the threshold of the 42 °C. (f) The average modulus corresponding to the temperature point of small-amplitude temperature sweep results. (g) Dynamic thermographic images of hydrogel/saline and (h) temperature profiles of monitoring points 2 and 3 of the hydrogel/saline group.

the time of the rabbit ablation procedure). The heater was maintained at 90 °C, 80 °C, and 70 °C respectively, and the temperature increases curves at each monitoring point of the hydrogel are shown in Fig. S11. As the externally set temperature decreased, heat conduction within the hydrogel slowed down, and the steady-state temperatures at 2 min of each monitoring point also decreased accordingly (Fig. 3e). In other words, the thermal insulation performance of the hydrogel is temperature dependent. The higher the external temperature, the higher the temperature inside the hydrogel, which likely related to the its high-water content. To investigate whether hydrogels can maintain their viscoelasticity when exposed to high temperatures. The rheological properties of hydrogels at different temperatures were investigated to gain insight into their performance under thermal stress (Fig. S12). Small-amplitude temperature step tests showed that the hydrogel maintained gel properties ($G'>G''$) as the temperature was increased from 25 to 95 °C (Fig. 3f). The entire test lasted 20–30 min, during which time the gel maintained its stability under thermal stress.

Dynamic thermography enables a more intuitive visualization of heat transfer in the hydrogel and saline, as illustrated in Fig. S13a. The two monitoring points were set at a distance of 7 mm from the edge of the iron block (Fig. S13b), which is comparable to the isolation distance created by the *in vivo* injection of the hydrogel. The hydrogel can maintain its morphology after placing a heated iron block (Fig. S13c,d), corroborating its thermal stability (Fig. 3f). In the hydrogel group (Fig. 3g, h; Fig. S13e, f), the images reveal that the hydrogel remains relatively cool: temperatures at No. 2 rose slowly from ~24 °C (0 s) to only ~29 °C (60 s), while No.3 likewise increased modestly to ~27 °C. The temperature curves exhibit a gradual, nearly linear incline over the full 60 s, without any abrupt jumps. By contrast, the saline group demonstrated rapid heat propagation (Fig. 3g, h; Fig. S13g, h). Both No. 2 and No. 3 temperatures surged to 60–70 °C within 5–6 s of heating. The images show a rapidly expanding “hot ring", indicating virtually unimpeded thermal conduction into the surrounding medium. Thus, hydrogel has superior insulating properties compared to saline.

When heated, the transfer of heat in water is mainly by thermal convection. The convective heat transfer coefficient of water is

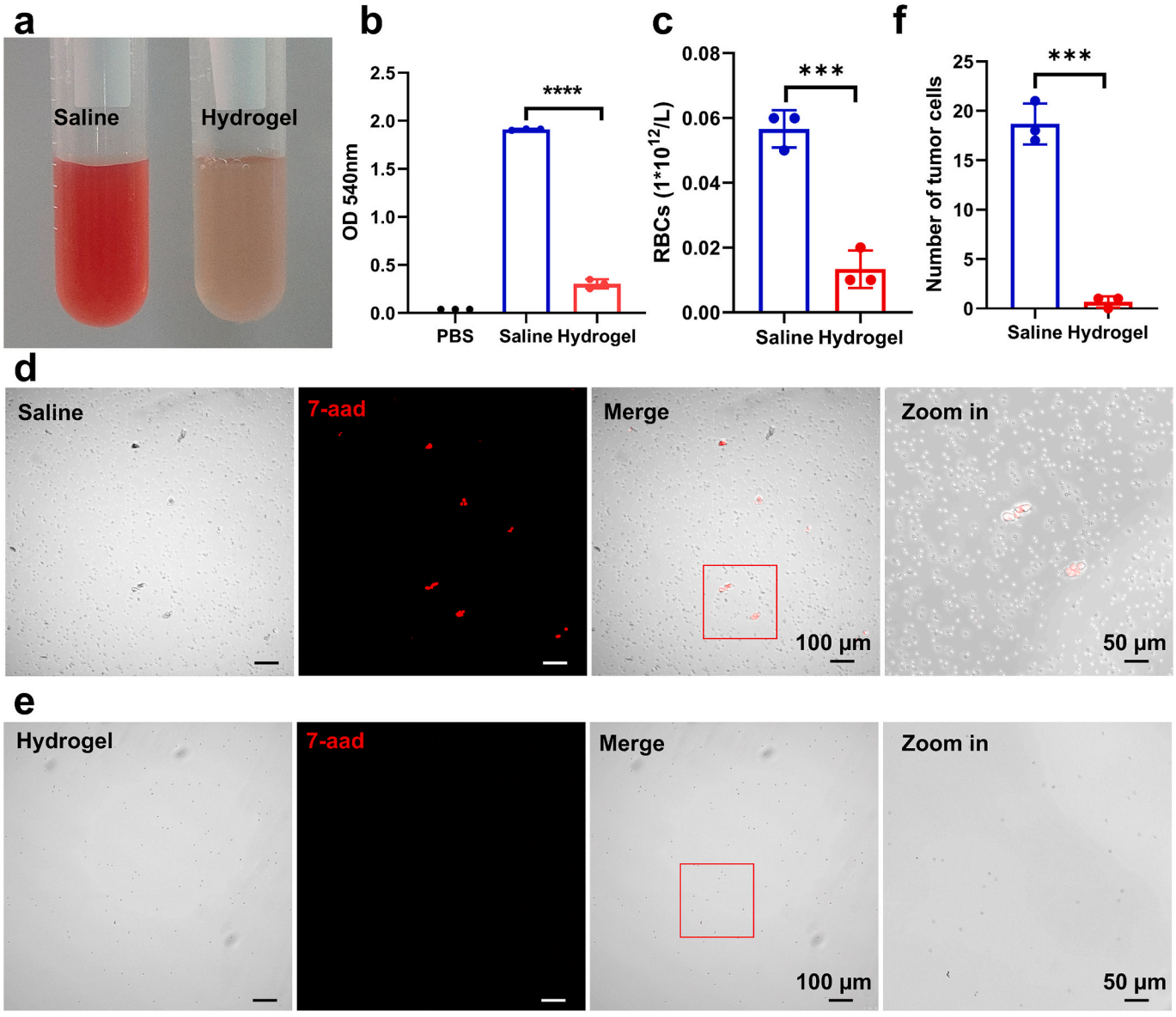

Fig. 4. Evaluation of the hemostatic properties of hydrogel. (a) Optical images of ascites collected postoperatively in the saline and the hydrogel groups. (b) Hemoglobin data of ascites at 540 nm using an enzyme marker. (c) Red blood cell counts in ascites detected by hematology analyzer. Fluorescence confocal images of (d)7-AAD labeled tumor cells and (e) normal red blood cells. (f) Quantitative data of tumor cells. The results are expressed as the mean ± SD in all groups ($n = 3$), where ns indicates no difference in data, $^{*}p < 0.05$, $^{**}p < 0.01$, $^{***}p < 0.001$.

estimated to be 100–1000 W/(m^2·K) for free convection, whereas it can range from 500 to 10,000 W/(m^2·K) for forced convection [45]. According to Fourier's law (1), the coefficient of thermal conductivity of hydrogel is 2.1621 W/(m•K). In fact, the heat transfer within the hydrogel may occur through thermal conduction accompanied with a minor thermal convection when heated. It is attributed to the 97.5 % water content of the hydrogel and the dynamic covalent bonding network. Therefore, the thermal conductivity calculated according to Fourier's formula is termed the "Equivalent Thermal Conductivity", a parameter encompassing both thermal conduction and convection. The thermoprotective properties of the hydrogel can also be explained by that PEG has a relatively high latent heat of fusion. In fact, the heat transfer within the hydrogel ought to be a pretty complicated variation, which might be a topic for in-depth research. In terms of this research, these results strongly support that the hydrogel is an exceptional alternative to saline isolator.

3.4. Evaluation of intraoperative hemostatic properties of the hydrogel

To verify the ability of the hydrogel to prevent leakage of blood cells and tumor cells, saline was injected intraperitoneally post-surgery and then ascites were collected for evaluation. Macroscopically, the saline group had significantly darker colored ascites (Fig. 4a) and a 6.29-fold increase in OD values compared to the hydrogel group (Fig. 4b). Hemoglobin analysis indicated a 4.25-fold higher hematocrit level in the saline group than in the hydrogel group (Fig. 4c). The levels of erythrocytes and tumor cells in the ascites were further assessed by staining. Free tumor cells with nuclei were labeled with 7-AAD, whereas erythrocytes remained unstained. A significantly higher number of erythrocytes and tumor cells in the saline group (Fig. 4d), with few free tumor cells observed in the hydrogel group (Fig. 4e). The count of tumor cells showed an 18.7-fold higher number of free tumor cells in the saline group than in the hydrogel group (Fig. 4f). The liquid saline can carry blood cells and tumor cells to other parts of the abdominal cavity during needle extraction with increased risk of tumor metastasis. Conversely, the hydrogel adheres to the surface of the liver while greatly reducing the leakage of blood cells and tumor cells during the procedure. This resulted in a lowered threat of tumor metastasis and improving substantial prognosis after thermal ablation. Considering the adhesive and self-healing properties of hydrogels, we believe that the function of hemostasis is mainly attributed to the self-healing property of hydrogel. In the process of needle extraction, the hydrogel can self-heal and seal the pinhole caused by the needle, thus physically sealing the bleeding produced during the puncture without assistance of medicines (*e.g.* hemostatic enzymes, *etc.*).

3.5. In vitro sealing test

Building on these findings, the sealing property of the hydrogel which is responsible for their hemostatic performance is evaluated. A

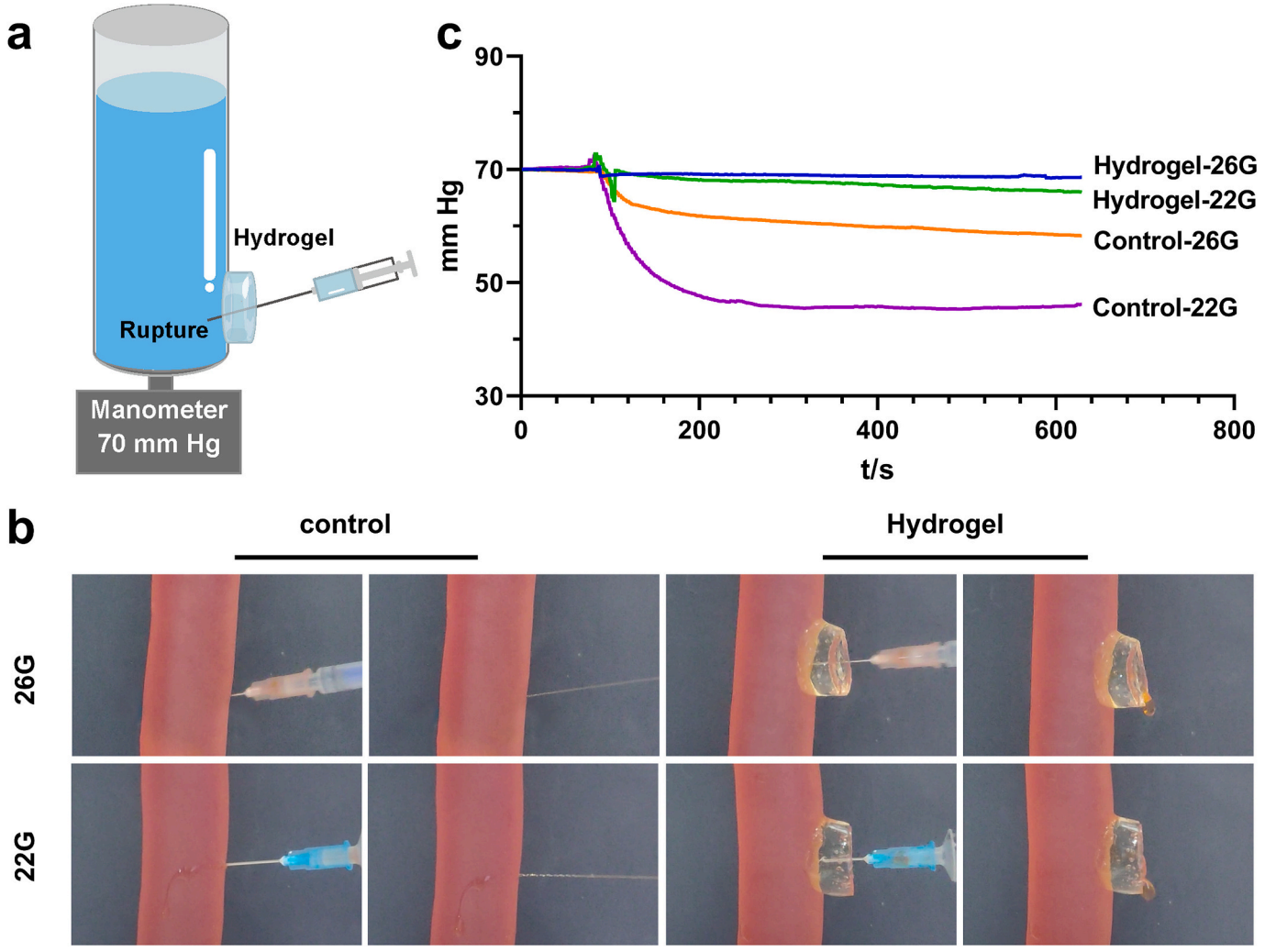

Fig. 5. *In vitro* sealing test. (a) *In vitro* sealing test model. (b) Images of the *in vitro* sealing test with control and hydrogel group, respectively. (c) Quantitative curves of pressure.

device based on a collagen shell was used for performing *in vitro* vascular simulation experiments (Fig. 5a). The collagen enteric coating was filled with PBS stained by acid orange 7 until the pressure reaches 70 mmHg. The shell was then punctured vertically in a downward position using needles of different gauges (Needle 22G and 26G). As shown in Fig. 5b, fluid immediately jetted out upon needle withdrawal in the unprotected group, while fluid leakage slowed significantly when the hydrogel was applied to the puncture site. This finding is corroborated by the manometer results (Fig. 5c) where unprotected collagen tubes exhibited an abrupt initial pressure drop, followed by gradual fluid loss over time. In contrast, hydrogel-protected tubes maintained pressure more effectively, with significantly slower fluid loss. The degree and rate of fluid leakage correlated closely with needle diameter, with the larger 22G needle (outer diameter 0.71 mm) causing faster and more extensive leakage compared to the smaller 26G needle (outer diameter 0.45 mm). Notably, even after puncture with the 22G needle, the hydrogel group only exhibited a minor pressure drop, underscoring the exceptional self-healing capacity of hydrogel. By rapidly sealing the puncture site and protecting the surrounding tissue, the hydrogel effectively reduces fluid loss and demonstrates outstanding protective performance. This sealing ability is particularly valuable in the context of *in vivo* puncture procedures, where it is expected to significantly mitigate the leakage of blood and tumor cells, thereby reducing the risk of abdominal adhesion and tumor metastasis. Moreover, it is worth noting that in clinical tumor puncture thermal ablation, large vessels are typically avoided, and bleeding is primarily caused by injury to the Glisson's capsule or small branches of the portal vein (pressure range: 5–10 mmHg) [46]. Given the relatively low pressures involved, the self-healing capability of hydrogel is sufficient to achieve effective sealing and hemostasis during puncture. This highlights the practical relevance of the hydrogel's sealing performance, reinforcing its potential as an efficient protective barrier during minimally invasive procedures.

3.6. In vivo evaluation of the hydrogel for postoperative anti-tumor metastasis

During the tumor ablation, cells leakage from the needle passage inevitably leads to tumor implantation. Conventional liquid saline is insufficient to prevent the dissemination of tumor cells into surrounding tissues and uncontrollable sites. The experiments on hemostasis have demonstrated that the sealing properties of the hydrogel can effectively mitigate this issue. To further evaluate the protective effect of hydrogel against tumor implantation, ultrasonography and histological evaluation of the postoperative ablation site were performed. Before the ablation procedure *in vivo*, no tumor implantation at the abdominal wall in either the saline or the hydrogel groups (Fig. S14). However, by the 6th postoperative day, an evident abdominal wall metastasis with a diameter of approximately 0.55 cm in the saline group was observed (Fig. 6a), whereas no tumor was detected in the hydrogel group (Fig. 6b). Subsequent dissection of the animal confirmed consistency with the ultrasound results.

Histological assessment, including H&E, Ki67, and MMP2 staining, was conducted on the metastatic tumor and abdominal wall tissue. H&E staining revealed numerous cells organized in nested clusters in the metastatic tumor tissue, displaying heterogeneous nuclei, high nucleoplasm ratios, prominent nucleoli, numerous mitotic figures (yellow arrows), and necrotic foci (red arrows) (Fig. 6c). In contrast, tissues from the hydrogel group displayed normal histological architecture with no evidence of tumor infiltration. High Ki67 expression is typically associated with high proliferative activity of tumor cells and worse prognosis. Thus, positive Ki67 staining indicated a malignant proliferative state and confirmed metastasis in the saline group (Fig. 6d). Additionally, MMP2, a key matrix metalloproteinase involved in extracellular matrix degradation and tumor cell invasion, was diffusely and strongly expressed in the saline group, while no significant expression was observed in the hydrogel group (Fig. S15). These findings collectively highlight the ability of hydrogel to act as an effective physical barrier, significantly reducing tumor cell leakage and subsequent implantation during thermal ablation. By minimizing the risk of postoperative metastasis and preserving tissue integrity, the hydrogel not only enhances the safety of thermal ablation but also contributes to improved long-term prognosis. This demonstrates the considerable potential of hydrogel as a multifunctional protective agent in oncological interventions, combining hemostatic sealing with anti-metastatic benefits.

3.7. In vivo evaluation of the hydrogel for postoperative anti-adhesion

Postoperative tissue adhesions are a common complication following thermal ablation, particularly at surgical contact sites such as the interfaces between the liver and intestine or the liver and peritoneum. Therefore, evaluating the anti-adhesive efficacy of the hydrogel after ablation is essential to assess its potential clinical benefits. On the 6th postoperative day, anatomical examination revealed extensive adhesions in the saline group, with firm connections formed between the abdominal wall and liver, as well as between the liver and intestinal wall (Fig. 7a); whereas no adhesions were observed in the hydrogel group (Fig. 7b). Consistently, the adhesion score in the saline group was significantly higher, reaching a score of 4, while the hydrogel group maintained a score of 0 (Fig. 7c). The major tissues were obtained and analyzed using H&E staining and Masson staining. There are multiple rhabdomyolysis (brown arrows) and massive connective tissue hyperplasia (green arrows) in the muscle layer; accompanied by minor inflammatory cell infiltration dominated by lymphocytes and granulocytes (blue arrows) in the saline group (Fig. 7d). While the hydrogel group displayed well-organized muscle fibers (yellow arrows), predominantly round cells, and an intact peritoneum (red arrows) without any pathological abnormalities. Masson staining can futher clearly show the presence of collagen deposition in the adhesion tissues involving the injured abdominal wall. The saline group had extensive collagen deposition, with significant connective tissue hyperplasia, inflammatory cell infiltration, and a larger fibrotic lesion area (Fig. 7e, f). Moreover, the adhesion band structure was loose, with visible capillaries (Fig. S16), reflecting more severe peritoneal adhesions. No obvious adhesion bands were observed in the hydrogel group, showing a well-preserved mesothelial structure with no evidence of adhesion band formation, indicating effective prevention of postoperative adhesions. Furthermore, abdominal wall injury can activate the NF-κB signaling pathway, leading to higher levels of excessive release of pro-inflammatory cytokines such as TNF-α. qPCR was performed to quantify TNF-α mRNA levels in locally adherent tissues (Fig. 7g). The TNF-α mRNA expression levels were remarkably 8.45-fold higher in the saline group than in the hydrogel group. Accordingly, the hydrogel effectively suppressed the inflammatory response triggered by thermal ablation-induced injury. Taken together, these findings demonstrate that the hydrogel not only serves as a physical barrier to prevent tissue adhesion, but also reduces excessive inflammatory responses at the injury site. This dual protective mechanism highlights the potential of hydrogel as an effective anti-adhesive and anti-inflammatory material, offering significant advantages for improving postoperative outcomes after thermal ablation procedures.

In addition, venous blood samples were collected to assess renal and hepatic function by measuring biomarkers, such as serum alanine aminotransferase (ALT), aspartate aminotransferase (AST), blood urea nitrogen (BUN) and creatinine (CREA). Compared to pre-treatment levels, ALT and AST levels in all groups postoperative were peaked on day 1, decreased on day 4 and decreased to normal levels on day 6 (Fig. 8a, b, Table S1 [47]). The peaks are due to the thermal impact and tumor ablation caused by MWA. The heat generated by MWA inevitably effects liver function while ablating the tumor cells. The slower decrease in ALT levels in the hydrogel group may relate to the metabolism of polymeric materials *in vivo* (Fig. 8a). Comparatively, the absorption of saline is very rapid. ALT levels have decreased to normal on day 6 in the

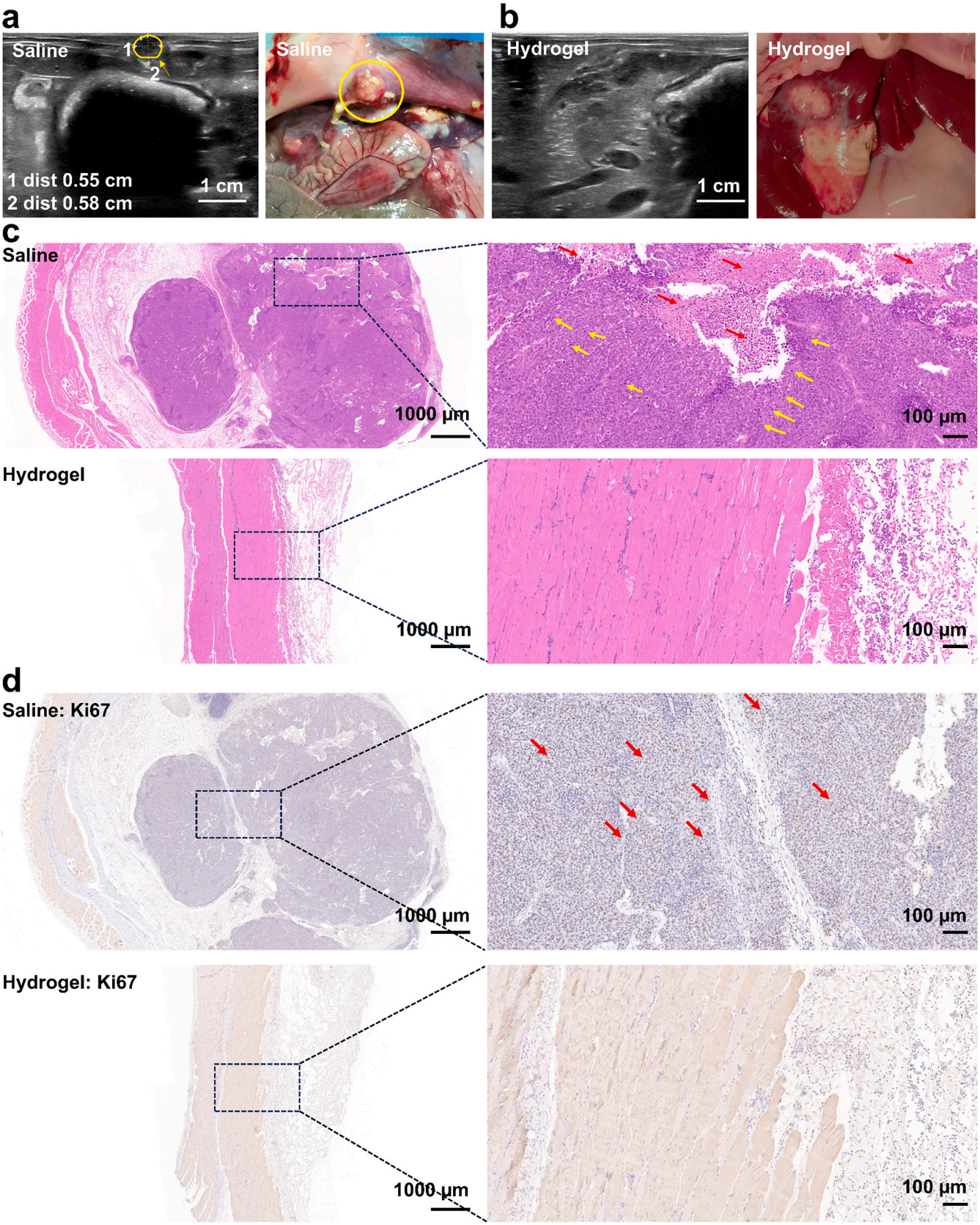

Fig. 6. The hydrogel prevents tumor metastasis in MWA therapy. Ultrasonic and optical images of (a) metastatic tumor on abdominal wall in the saline group, and (b) the normal abdominal wall in the hydrogel group. Scale bar:1 cm. (c) H&E staining of metastatic tumor in the saline group and the normal abdominal wall in the hydrogel group. (d) Ki67 immunostaining of metastatic tumor in the saline group and abdominal wall in the hydrogel group.

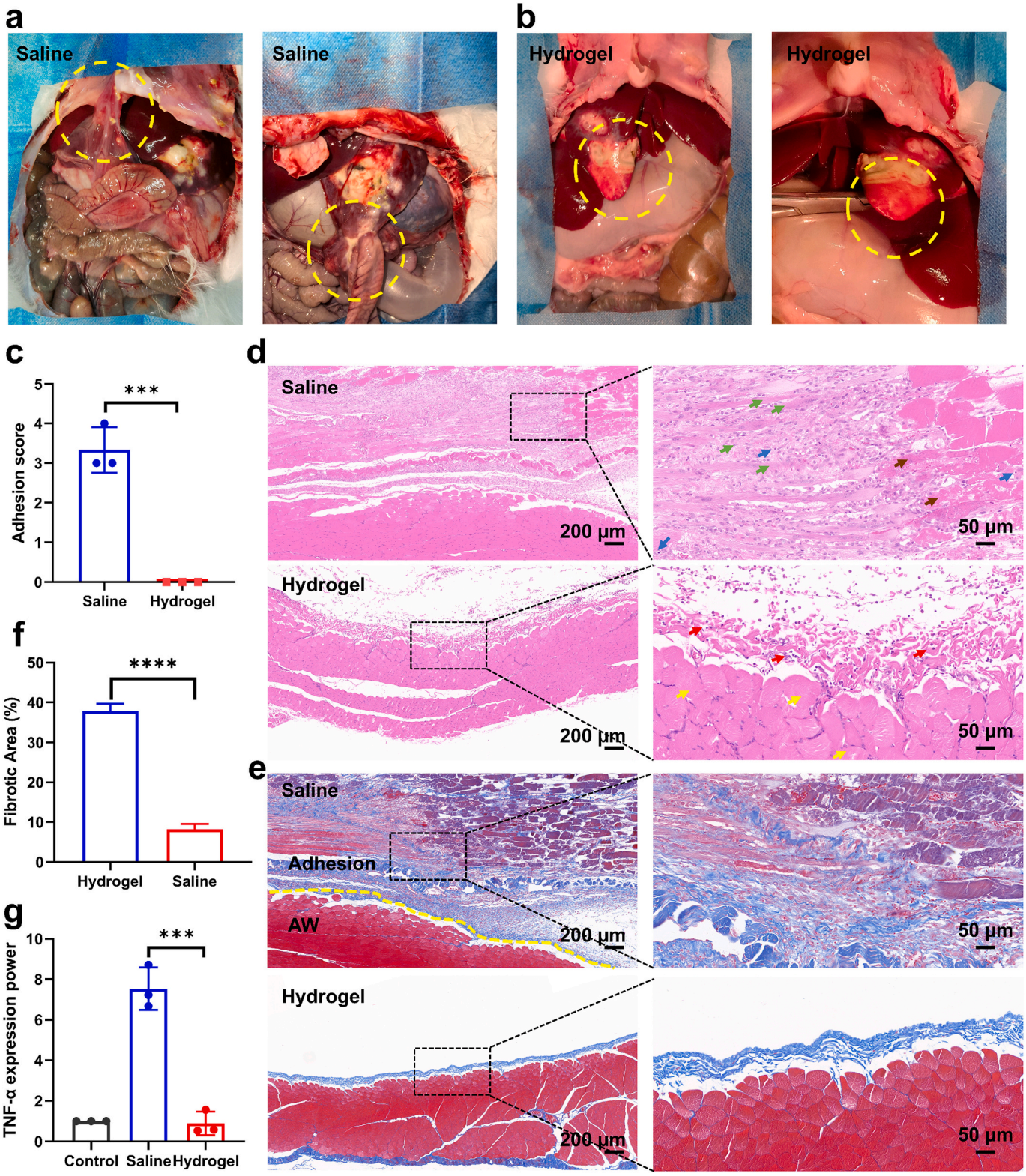

Fig. 7. The hydrogel prevents adhesions after MWA therapy. Optical images of the postoperative abdominal cavity in the saline group (a) and hydrogel group (b). (c) Scoring of the degree of adhesions. The results are expressed as the mean ± SD in all groups ($n = 3$). (d) H&E staining of abdominal wall tissue of saline group and hydrogel group. (e) Masson staining of abdominal wall tissue of saline group and hydrogel group. (f) Quantitative percentage of fibrotic tissue area. The results are expressed as the mean ± SD in all groups (n = 3). (g) The expression level of TNF-α mRNA in abdominal wall tissue. The results are expressed as the mean ± SD in all groups (n = 3). *$p < 0.05$, **$p < 0.01$, ***$p < 0.001$.

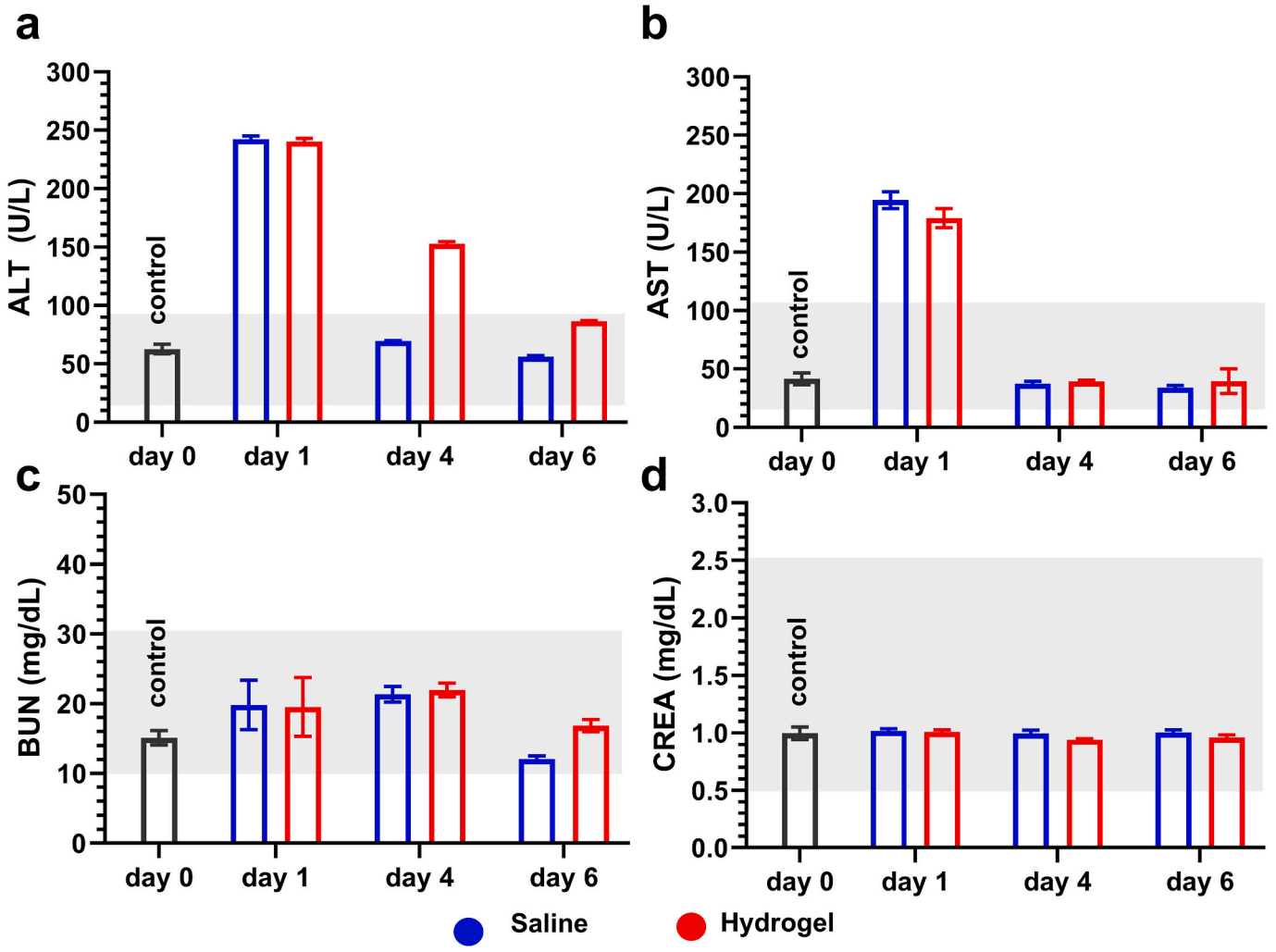

Fig. 8. Blood biochemical analysis of rabbits after MWA treatment. Biomarkers include (a) alanine aminotransferase (ALT), (b) aspartate aminotransferase (AST), (c) urea (BUN) and (d) creatinine (CREA). The gray shading indicates the normal interval of the biochemical values. The results are expressed as the mean ± SD in all groups (Control, $n = 6$, other group, $n = 3$).

hydrogel group. BUN and CREA are often used to evaluate renal function. BUN levels fluctuated in both groups, but remained within normal ranges (Fig. 8c), likely influenced by factors such as circadian rhythms, diet, liver function, hydration and intestinal absorption. CREA had no significantly change in either group (Fig. 8d), suggesting that renal function was not impaired in the treated rabbits. To sum up, these results demonstrate that the hydrogel not only provides effective thermal protection, hemostasis, anti-metastasis, and anti-adhesion benefits during MWA, but also does so without inducing detectable hepatic or renal toxicity. This comprehensive safety profile, combined with its multifunctional therapeutic effects, highlights the significant potential of hydrogel as a superior alternative to saline for improving the safety and efficacy of thermal ablation procedures.

4. Conclusion

We prepared a chitosan-PEG-based self-healing chitosan hydrogel and validated its versatile roles in a thermal ablation model of highly metastatic VX2 tumors, including thermoprotection, hemostasis, anti-tumor metastasis and anti-adhesion, which called “one stone, four birds” strategy. The hydrogel exhibited injectability, good self-healing, shape adaptation, hemocompatibility and cytocompatibility. Especially, the dynamic Schiff base imparts a solid yet dynamic state that is superior to flowing saline. It adhered stably to the surface of the damaged tissue, thus providing superior thermal protection in percutaneous liver tumor ablation of rabbits, and effectively preventing blood and tumor cell leakage. These performances hence reduce abdominal tumor metastasis and potently avoid intraperitoneal adhesions. This hydrogel greatly optimizes clinical treatment strategies for highly metastatic tumors and reduces the rate of local tumor recurrence. Hence, the self-healing chitosan hydrogel is a promising thermal protective agent, which can also play the important roles of postoperative anti-tumor metastasis and anti-tissue adhesion after thermal ablation treatment to improve postoperative prognosis and allow for clinical practice. Future comprehensive large-animal studies and further optimization of the adhesion and sealing of hydrogels are expected to move toward clinical translation. Additionally, it has high potential to further carry anesthetics, painkillers, and anticancer agents in clinical, providing

analgesic and anti-tumor effects postoperatively, thereby contributing to improved postoperative management.

Supplementary data to this article can be found online at https://doi.org/10.1016/j.ijbiomac.2025.144187.

CRediT authorship contribution statement

Lifei Huang: Writing – original draft, Visualization, Methodology, Investigation, Data curation. **Erpeng Qi:** Methodology, Investigation, Data curation. **Zhihan Liu:** Validation, Investigation. **Quanrui Zhang:** Validation, Investigation. **Shuo Wang:** Data curation. **Shaowei Zheng:** Data curation. **Wensheng Xie:** Formal analysis. **Guofeng Li:** Methodology, Formal analysis. **Xue Chen:** Methodology, Formal analysis. **Hui Sun:** Supervision, Resources, Conceptualization. **Fangyi Liu:** Supervision, Resources, Funding acquisition, Conceptualization. **Xing Wang:** Writing – review & editing, Supervision, Funding acquisition, Conceptualization.

Declaration of competing interest

The authors declare that they have no known competing financial interests or personal relationships that could have appeared to influence the work reported in this paper.

Acknowledgments

This work was supported by Key Program of Beijing Natural Science Foundation (grant number Z200025), National Natural Science Foundation of China (grant number 52273118, grant number 22275013, grant number 82171940), and Fundamental Research Funds for the Central Universities (grant number QNTD2023-01).

Data availability

Data will be made available on request.

References

[1] M. Ahmed, C.L. Brace, F.T. Lee, et al., Principles of and advances in percutaneous ablation[J], Radiology 258 (2) (2011) 351–369.
[2] F. Zhu, H. Rhim, Thermal ablation for hepatocellular carcinoma: what's new in 2019: 6[J], Chin. Clin. Oncol. 8 (6) (2019) 58.
[3] L. Crocetti, T. De Baére, P.L. Pereira, et al., CIRSE standards of practice on thermal ablation of liver tumours[J], Cardiovasc. Intervent. Radiol. 43 (7) (2020) 951–962.
[4] H. Takahashi, E. Berber, Role of thermal ablation in the management of colorectal liver metastasis[J], Hepatobiliary Surg. Nutr. 9 (1) (2020) 49–58.
[5] Y. Choi, S.-L. Jung, Efficacy and safety of thermal ablation techniques for the treatment of primary papillary thyroid microcarcinoma: a systematic review and meta-analysis[J], Thyroid® 30 (5) (2020) 720–731.
[6] F. Izzo, V. Granata, R. Grassi, et al., Radiofrequency ablation and microwave ablation in liver tumors: an update[J], Oncologist 24 (10) (2019) e990–e1005.
[7] S. Shiina, K. Sato, R. Tateishi, et al., Percutaneous ablation for hepatocellular carcinoma: comparison of various ablation techniques and surgery[J], Can. J. Gastroenterol. Hepatol. 1 (2018) 4756147.
[8] N.V. Violi, R. Duran, B. Guiu, et al., Efficacy of microwave ablation versus radiofrequency ablation for the treatment of hepatocellular carcinoma in patients with chronic liver disease: a randomised controlled phase 2 trial[J], Lancet Gastroenterol. Hepatol. 3 (5) (2018) 317–325.
[9] Y. Zhou, Y. Yang, B. Zhou, et al., Challenges facing percutaneous ablation in the treatment of hepatocellular carcinoma: extension of ablation criteria[J], J. Hepatocell. Carcinoma 8 (2021) 625–644.
[10] Y. Min, X. Wang, H. Chen, et al., Thermal ablation for papillary thyroid microcarcinoma: how far we have come?[J], Cancer Manag. Res. 12 (2020) 13369–13379.
[11] K. Leuchte, E. Staib, M. Thelen, et al., Microwave ablation enhances tumor-specific immune response in patients with hepatocellular carcinoma[J], Cancer Immunol. Immunother. 70 (4) (2021) 893–907.
[12] B. Radjenović, M. Sabo, L. Šoltes, et al., On efficacy of microwave ablation in the thermal treatment of an early-stage hepatocellular carcinoma: 22[J], Cancers 13 (22) (2021) 5784.
[13] S. Nieuwenhuizen, M. Dijkstra, R.S. Puijk, et al., Microwave ablation, radiofrequency ablation, irreversible electroporation, and stereotactic ablative body radiotherapy for intermediate size (3–5 cm) unresectable colorectal liver metastases: a systematic review and meta-analysis[J], Curr. Oncol. Rep. 24 (6) (2022) 793–808.
[14] J. Zhao, Q. Li, M. Muktiali, et al., Effect of microwave ablation treatment of hepatic malignancies on serum cytokine levels[J], BMC Cancer 20 (1) (2020) 812.
[15] N.H. Shaheen, A.D. Hardie, Approach to hepatic tumor ablation: choosing the right tool for the job[J], Acad. Radiol. 31 (4) (2024) 1302–1303.
[16] K.B. Gala, N.S. Shetty, P. Patel, et al., Microwave ablation: how we do it?[J], Indian J. Radiol. Imaging 30 (2) (2020) 206–213.
[17] T.J. Vogl, N.-E.A. Nour-Eldin, R.M. Hammerstingl, et al., Microwave ablation (MWA): basics, technique and results in primary and metastatic liver neoplasms–review article[J], RöFo-Fortschritte auf dem Gebiet der Röntgenstrahlen und der bildgebenden Verfahren 189 (11) (2017) 1055–1066.
[18] P. Liang, Y. Wang, X. Yu, et al., Malignant liver tumors: treatment with percutaneous microwave ablation—complications among cohort of 1136 patients [J], Radiology 251 (3) (2009) 933–940.
[19] R.Z. Swan, D. Sindram, J.B. Martinie, et al., Operative microwave ablation for hepatocellular carcinoma: complications, recurrence, and long-term outcomes[J], J. Gastrointest. Surg. 17 (4) (2013) 719–729.
[20] C. Fang, K. Cortis, G.T. Yusuf, et al., Complications from percutaneous microwave ablation of liver tumours: a pictorial review[J], Br. J. Radiol. 92 (1099) (2019) 20180864.
[21] W. Tan, Q. Deng, S. Lin, et al., Comparison of microwave ablation and radiofrequency ablation for hepatocellular carcinoma: a systematic review and meta-analysis[J], Int. J. Hyperth. 36 (1) (2019) 263–271.
[22] S. Zensen, A. Bücker, M. Meetschen, et al., Current use of percutaneous image-guided tumor ablation for the therapy of liver tumors: lessons learned from the registry of the German Society for Interventional Radiology and Minimally Invasive Therapy (DeGIR) 2018–2022[J], Eur. Radiol. 34 (5) (2024) 3322–3330.
[23] Z. Yanna, Jun Liu, H. Li, et al., Safety of normal saline isolation zone: an experimental study on laser, radiofrequency and microwave thyroid thermal ablation[J], J. Surg. Concept Pract. 25 (05) (2020) 432.
[24] J. Wu, Z.-L. Zhao, X.-J. Cao, et al., A feasibility study of microwave ablation for papillary thyroid cancer close to the thyroid capsule[J], Int. J. Hyperth. 38 (1) (2021) 1217–1224.
[25] A. Pfannenstiel, J. Sebek, H. Fallahi, et al., Directional microwave ablation: experimental evaluation of a 2.45-ghz applicator in ex vivo and in vivo liver[J], J. Vasc. Interv. Radiol. 31 (7) (2020), 1170–1177.e2.
[26] M. Ozen, D. Raissi, Current perspectives on microwave ablation of liver lesions in difficult locations[J], J. Clin. Imaging Sci. 12 (2022) 61.
[27] J. Garnon, R.L. Cazzato, J. Caudrelier, et al., Adjunctive thermoprotection during percutaneous thermal ablation procedures: review of current techniques[J], Cardiovasc. Intervent. Radiol. 42 (3) (2019) 344–357.
[28] G. Tsoumakidou, X. Buy, J. Garnon, et al., Percutaneous thermal ablation: how to protect the surrounding organs[J], Tech. Vasc. Interv. Radiol. 14 (3) (2011) 170–176.
[29] A. Radosevic, R. Quesada, C. Serlavos, et al., Microwave versus radiofrequency ablation for the treatment of liver malignancies: a randomized controlled phase 2 trial[J], Sci. Rep. 12 (1) (2022) 316.
[30] L. Feng, Y. Wang, L.J. Niu, Ultrasound-guided percutaneous thermal ablation assisted by artificial ascites and soft tissue edema in the treatment of special-region hepatic tumors[J], Zhonghua Zhong liu za zhi [Chinese Journal of Oncology] 46 (2) (2024) 155–160.
[31] P. Namakshenas, A. Mojra, Optimization of polyethylene glycol-based hydrogel rectal spacer for focal laser ablation of prostate peripheral zone tumor[J], Physica Medica 89 (2021) 104–113.
[32] K. Liu, M. Russo, J.S. Ellis, et al., Transient, image-guided gel-dissection for percutaneous thermal ablation[J], Adv. Healthc. Mater. (2024) 2400272.
[33] L. Huang, S. Yang, M. Bai, et al., Thermal shielding performance of self-healing hydrogel in tumor thermal ablation[J], Colloids Surf. B: Biointerfaces 213 (2022) 112382.
[34] T. Narukawa, A. Fujihara, A. Ochiai, et al., Role of hydrogel spacer to protect the rectum from thermal injury in focal therapy of prostate cancer: preclinical study in cadaver model[J], Int. J. Urol. 30 (1) (2023).
[35] L.-L. Zhang, G.-M. Xia, Y.-J. Liu, et al., Effect of a poloxamer 407-based thermosensitive gel on minimization of thermal injury to diaphragm during microwave ablation of the liver[J], World J. Gastroenterol. 23 (12) (2017) 2141–2148.
[36] Y. Cao, Y. Zhou, J. Pan, et al., A general strategy towards an injectable microwave-sensitive immune hydrogel for combined percutaneous microwave ablation and immunotherapy[J], Chem. Eng. J. 422 (2021) 130111.
[37] B. Zheng, P. Zhang, Q. Lv, et al., Development and preclinical evaluation of multifunctional hydrogel for precise thermal protection during thermal ablation [J], Bioact. Mater. (31) (2024) 119–135.
[38] Y. Fu, Y. Li, B. Deng, et al., Spatiotemporally dynamic therapy with shape-adaptive drug-gel for the improvement of tissue regeneration with ordered structure[J], Bioact. Mater. (8) (2022) 165–176.
[39] S.H. Kim, K. Kim, B.S. Kim, et al., Fabrication of polyphenol-incorporated anti-inflammatory hydrogel via high-affinity enzymatic crosslinking for wet tissue adhesion[J], Biomaterials 242 (2020) 119905.
[40] F. Pascale, J.P. Pelage, M. Wassef, et al., Rabbit VX2 liver tumor model: a review of clinical, biology, histology, and tumor microenvironment characteristics[J], Front. Oncol. 12 (2022) 871829.
[41] X. Duan, G. Zhou, C. Zheng, et al., Heat shock protein 70 expression and effect of combined transcatheter arterial embolization and radiofrequency ablation in the rabbit vx2 liver tumour model[J], Clin. Radiol. 69 (2) (2014) 186–193.

[42] H. Li, P. Chen, M. Wang, et al., Liposome quercetin enhances the ablation effects of microwave ablation in treating the rabbit vx2 liver tumor model[J], Int. J. Hyperth. 39 (1) (2022) 162–172.
[43] H. Kimura, N. Shibuya, Y. Kimura, Hydrogen sulfide is a signaling molecule and a cytoprotectant[J], Antioxid. Redox Signal. 17 (1) (2012) 45–57.
[44] H. Kimura, Signaling molecules: hydrogen sulfide and polysulfide[J], Antioxid. Redox Signal. 22 (5) (2015) 362–376.
[45] P.K. Jain, Taking the heat off of plasmonic chemistry[J], J. Phys. Chem. C 123 (40) (2019) 24347–24351.
[46] A.L. Baert, Portal Hypertension: Diagnostic Imaging and Imaging-Guided Therapy, Springer Science & Business Media, 2012.
[47] M. Washington I, G. Van Hoosier, Clinical biochemistry and hematology[M]//The laboratory rabbit, guinea pig, hamster, and other rodents, Academic Press (2012) 57–116.